# Broadband inversion for MAS NMR with single-sideband-selective adiabatic pulses

Andrew J. Pell,[1] Gwendal Kervern,[1] Lyndon Emsley,[1] Michaël Deschamps,[2] Dominique Massiot,[2] Philip J. Grandinetti,[3] and Guido Pintacuda[1,a)]
[1]*Université de Lyon, Centre de RMN à Très Hauts Champs, FRE 3008 CNRS/Ecole Normale Supérieure de Lyon/Université Claude Bernard Lyon 1, 69100 Villeurbanne, France*
[2]*CEMHTI CNRS UPR3079 and Université d'Orléans, 1D, Avenue de la Recherche Scientifique, 45071 Orléans Cedex 2, France*
[3]*Department of Chemistry, Ohio State University, 100 West 18th Avenue, Columbus, Ohio 43210, USA*

(Received 24 August 2010; accepted 9 November 2010; published online 13 January 2011)

We explain how and under which conditions it is possible to obtain an efficient inversion of an entire sideband family of several hundred kHz using low-power, sideband-selective adiabatic pulses, and we illustrate with some experimental results how this framework opens new avenues in solid-state NMR for manipulating spin systems with wide spinning-sideband (SSB) manifolds. This is achieved through the definition of the criteria of phase and amplitude modulation for designing an adiabatic inversion pulse for rotating solids. In turn, this is based on a framework for representing the Hamiltonian of the spin system in an NMR experiment under magic angle spinning (MAS). Following earlier ideas from Caravatti *et al.* [J. Magn. Reson. **55**, 88 (1983)], the so-called "jolting frame" is used, which is the interaction frame of the anisotropic interaction giving rise to the SSB manifold. In the jolting frame, the shift modulation affecting the nuclear spin is removed, while the Hamiltonian corresponding to the RF field is frequency modulated and acquires a spinning-sideband pattern, specific for each crystallite orientation. © *2011 American Institute of Physics*. [doi:10.1063/1.3521491]

## I. INTRODUCTION

Over the last 20 years, impressive progress in magnet and magic angle spinning (MAS) probe technology and radio frequency (RF) irradiation schemes has revolutionized the solid-state NMR field, opening it to the structural characterization of a large variety of systems in many areas of modern chemistry, biology, and material sciences.[1–4]

One key barrier to further progress in the studies of several classes of new substrates is represented by the difficulty to excite and invert signals with extremely large shifts and shift anisotropies. One possible solution to achieving broadband inversion is to use swept-frequency adiabatic pulses which are widely used in solution state experiments, for instance, for facilitating heteronuclear decoupling,[5–8] or in many applications in magnetic resonance imaging.[9] These pulses give very high bandwidths in relation to the RF power used, and have been shown to be very tolerant of instrumental imperfections such as spatial inhomogeneity of the RF field.[9,10]

A broad palette of MAS experiments involving adiabatic pulses has recently been proposed in solid-state NMR. Applications embrace widely different areas, from biological macromolecules,[11] to paramagnetic solids.[12] Even more recently, the use of adiabatic pulses has gained interest in the field of NMR of quadrupolar nuclei under MAS. Wasylishen *et al.*[13–15] have demonstrated an intriguing new application showing that the irradiation of a single sideband of a satellite transition with a hyperbolic–secant pulse[16] can result in complete inversion of the entire sideband pattern, resulting in an enhancement of the signal of the central transition. It has also been shown[17] that the use of a WURST pulse[7] can provide an even greater enhancement of this transition. This opens completely new perspectives for the use of adiabatic pulses in solids, where they can deliver an even more broadband excitation than in solution.

Despite this flourishing literature on new experimental schemes, no theoretical description of adiabatic pulses under MAS has been proposed so far. The treatment of adiabatic pulses in rotating solids is not straightforward, as the picture is deeply perturbed by the shift modulation imposed by the sample rotation. Consequently, in solids, the "modulated frame" approach,[16] which is commonly employed in solution-state NMR, provides a good description only in the limit of moderate shift anisotropies or of moderate spinning speeds,[11] or in the case of the short high-power adiabatic pulses (SHAPs).[12]

In the following, we introduce a framework for representing the Hamiltonian of the spin system in an NMR experiment under MAS. Following earlier ideas from Caravatti *et al.*,[18] we use here the so-called "jolting frame," which is the frame of the anisotropic interaction giving rise to the spinning sideband (SSB) manifold. In the jolting frame, the shift modulation affecting the nuclear spin is removed, while the Hamiltonian corresponding to the RF field is frequency modulated and acquires a SSB pattern, specific for each crystallite orientation.

This representation allows to easily define the criteria of phase and amplitude modulation for designing an adiabatic inversion pulse in rotating solids. Notably, we demonstrate

a)Author to whom correspondence should be addressed. Electronic mail: Guido.Pintacuda@ens-lyon.fr.

 

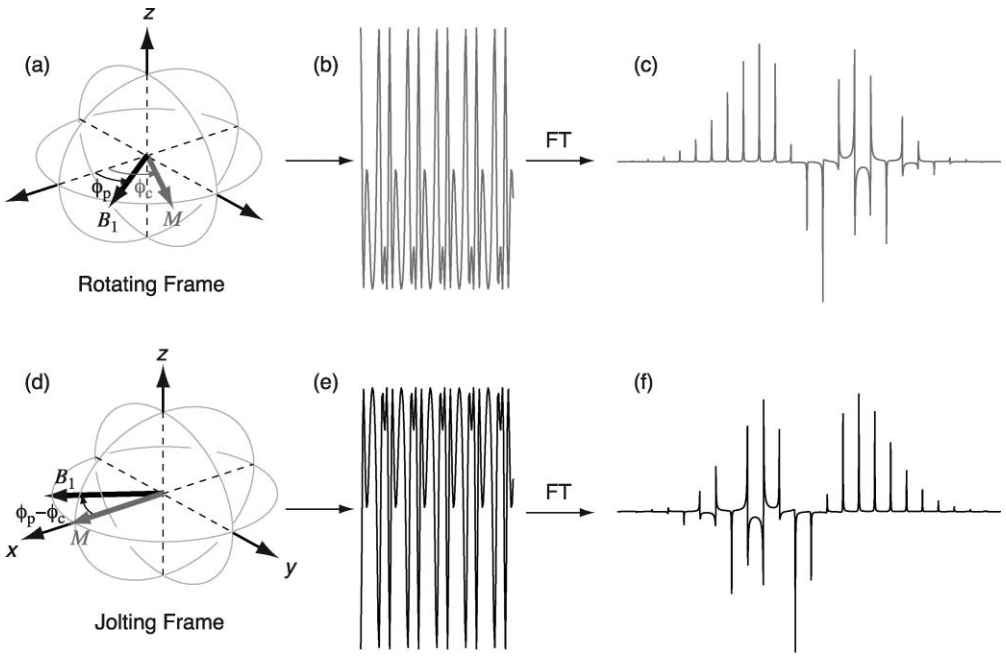


FIG. 1. Fourier decomposition of the $B_1$ field in the rotating and jolting frames. (a) shows the evolution of the magnetization in the rotating frame, which gives the FID in (b). The Fourier transform of this trajectory gives a sideband pattern (c). The representation of $B_1$ in the jolting frame (d) produces a trajectory which is the conjugate of the FID (e), therefore its Fourier transform gives a mirror image spectrum (f).

that the ratio between the RF power and the achieved bandwidth under MAS can be even more impressive than the solution-state counterpart, showing that efficient inversion of entire sideband families of several hundred kHz can be achieved using low-power (10–60 kHz), single-sideband-selective adiabatic pulses.

## II. THE JOLTING FRAME

### A. General principle

Generally, most NMR experiments are evaluated in the so-called "rotating frame," which is a frame of reference which rotates about the $z$-axis of the laboratory frame at the RF carrier frequency $\omega_{rf}$. This is convenient because the resonant component $B_1$ of the RF field is stationary with a phase $\varphi_p$, and the magnetization $M$ appears to evolve under a reduced magnetic field at the offset frequency $\Omega_c$,[19] producing the free induction decay (FID). In a solid-state experiment under MAS, the rotation of the sample imposes a periodic time modulation of the anisotropic part of the Hamiltonian (e.g., the chemical shift anisotropy), which gives rise to an oscillating motion of the magnetization about the reduced magnetic field along $z$, and acquires a periodic phase $\varphi_c(t)$ in addition to the phase due to the isotropic shift. The oscillatory part results in a spectrum comprising a series of sidebands separated by the MAS frequency. This is shown in Figs. 1(a)–1(c).

The "jolting frame" is a rotating frame following the evolution of the magnetization during a period of free precession. In this frame, the apparent chemical shift is zero at all times, and the $B_1$ field acquires a phase $-\varphi_c(t)$ in addition to $\varphi_p$, and so it appears to evolve at the negative of the chemical shift as measured in the rotating frame. The representation of $B_1$ in the jolting frame [Fig. 1(e)] corresponds to the time reversal of the FID in panel (b), and its Fourier transform panel (f) gives a sideband pattern which is the mirror image of that encoded in the FID panel (c).

### B. Interaction representation of the shift anisotropy

The idea of single-sideband irradiation was first proposed by Caravatti *et al.*[18] who used a selective DANTE sequence[20,21] to selectively invert a single sideband under moderate MAS frequencies.

For the present purpose, we can restrict the discussion to a single spin $I$ with a shift anisotropy (SA) tensor in a single crystallite. This interaction is modulated during MAS by the function $\Omega_c(t)$ which is given by:[22]

$$\Omega_c(t) = \sum_{k=-2}^{+2} \omega_k(\alpha, \beta, \gamma) \exp(-ik\omega_r t), \tag{1}$$

where the coefficients $\omega_k(\alpha, \beta, \gamma)$ are given by:

$$\omega_k(\alpha, \beta, \gamma) = \sqrt{\frac{2}{3}} \sum_{k'=-2}^{+2} \rho_{2k'} \exp(-ik'\alpha) d^2_{k'k}(\beta) \times \exp(-ik\gamma) d^2_{k0}(\theta_M) + \Omega_{iso}\delta_{k0}. \tag{2}$$

The Euler angles $(\alpha, \beta, \gamma)$ relate the principal axis frame (PAF) of the SA tensor to the rotor frame, and $d^2_{k'k}(\theta)$ are the elements of the reduced Wigner rotation matrices. The angle between the rotor axis and the external magnetic field $B_0$ is the magic angle $\theta_M$, which has value arctan $(\sqrt{2})$. Finally, the spatial components of the SA tensor in the PAF are given by $\rho_{2k}$, which in terms of the principal Cartesian values $\sigma_{ii}$ in the

PAF are:

$$\rho_{20} = -\sqrt{\tfrac{3}{2}}\omega_0(\sigma_{zz} - \sigma_{\rm iso}) = \sqrt{\tfrac{3}{2}}\Delta, \tag{3}$$

$$\rho_{2\pm1} = 0, \tag{4}$$

$$\rho_{2\pm2} = -\tfrac{1}{2}\omega_0(\sigma_{xx} - \sigma_{yy}) = -\tfrac{1}{2}\eta\Delta, \tag{5}$$

where $\omega_0 = -\gamma_I B_0$ is the Larmor frequency of the spin, $\gamma_I$ is the gyromagnetic ratio, and $\sigma_{\rm iso}$ is the isotropic shielding, which is given by

$$\sigma_{\rm iso} = \tfrac{1}{3}(\sigma_{xx} + \sigma_{yy} + \sigma_{zz}). \tag{6}$$

Thus, the interaction is described in terms of the anisotropy $\Delta = -\omega_0(\sigma_{zz} - \sigma_{\rm iso})$, the asymmetry $\eta = (\sigma_{xx} - \sigma_{yy})/(\sigma_{zz} - \sigma_{\rm iso})$, and an isotropic shift which, in the rotating reference frame, is given by $\Omega_{\rm iso} = \omega_0(1 - \sigma_{\rm iso}) + \omega_{\rm rf}$, where $\omega_{\rm rf} = -\omega_0$ (for $\gamma > 0$) is the carrier frequency of the RF transmitter (which coincides with the receiver reference frequency).

If we apply a radio frequency pulse with field $\omega_1$ and time-dependent phase $\phi_{\rm p}(t)$, the Hamiltonian is given by

$$\hat{H}(t) = \Omega_{\rm c}(t)\hat{I}_z + \omega_1 \hat{R}_z(\phi_{\rm p}(t))\hat{I}_x \hat{R}_z(\phi_{\rm p}(t))^{-1}, \tag{7}$$

where $\hat{I}_i$ is the component of the $I$-spin angular momentum along axis $i$, and $\hat{R}_z(\theta)$ is the operator representing a rotation of the spin through angle $\theta$ about the $z$-axis. We now transform into the jolting frame, which follows the evolution of the magnetization that is due to the anisotropic shift, resulting in the removal of the term in $\hat{I}_z$. However, this time dependence is transferred to the RF term, thus giving the phase of the pulse an additional time-dependent term. The operator representing the transformation is $\hat{V}(t) = \exp(-{\rm i}\phi_{\rm c}(t)\hat{I}_z)$ where

$$\phi_{\rm c}(t) = \Omega_{\rm iso}t + \int_0^t \sum_{k\neq0} \omega_k(\alpha, \beta, \gamma)\exp(-{\rm i}k\omega_{\rm r}t')\,{\rm d}t' \tag{8}$$

is the phase accumulated due to the evolution of the shift. In this frame, the Hamiltonian becomes:

$$\begin{aligned}\hat{\tilde{H}}(t) &= \hat{V}(t)^{-1}\hat{H}(t)\hat{V}(t) - \Omega_{\rm c}(t)\hat{I}_z \\ &= \omega_1 \hat{R}_z(\phi_{\rm p}(t) - \phi_{\rm c}(t))\hat{I}_x \hat{R}_z(\phi_{\rm p}(t) - \phi_{\rm c}(t))^{-1}.\end{aligned} \tag{9}$$

As shown by Caravatti *et al.*, the above expression can be rewritten to give a very useful result.[18] It is well known that during a period of free precession the magnetization of a particular spin, as measured in the rotating frame, is split into a series of components. Each component evolves at a frequency that deviates from the isotropic shift by a multiple of the spinning frequency, and thus the whole series gives a set of spinning sidebands. In operator notation, this can be represented as

$$\begin{aligned}\hat{R}_z(\phi_{\rm c}(t))\hat{I}_x \hat{R}_z(\phi_{\rm c}(t))^{-1} = \sum_{m=-\infty}^{+\infty} A_m \hat{R}_z(\phi_m + (\Omega_{\rm iso} + m\omega_{\rm r})t) \\ \times \hat{I}_x \hat{R}_z(\phi_m + (\Omega_{\rm iso} + m\omega_{\rm r})t)^{-1},\end{aligned} \tag{10}$$

where $A_m$ and $\phi_m$ are the intensity and phase of the $m$th sideband. These complex sideband intensities are Fourier coefficients, which are given by the integral expression:

$$\begin{aligned}&A_m \exp({\rm i}\phi_m) \\ &= \frac{1}{\tau_{\rm r}}\int_0^{\tau_{\rm r}} \exp\left[-\sum_{k\neq0}\frac{\omega_k(\alpha, \beta, \gamma)(\exp(-{\rm i}k\omega_{\rm r}t) - 1)}{k\omega_{\rm r}}\right] \\ &\quad \times \exp(-{\rm i}m\omega_{\rm r}t)\,{\rm d}t,\end{aligned} \tag{11}$$

where $\tau_{\rm r} = 2\pi/\omega_{\rm r}$ is one rotor period. It proves useful at this point to introduce the concept of a carousel of crystallites,[23] which is the set of crystallites that occupy the same positions during sample rotation, but at different times. For a powdered sample, such crystallites share the same values of the Euler angles $\alpha$ and $\beta$, but have different Euler angles $\gamma$. This behavior allows us to derive the variation of the sideband intensities and phases with $\gamma$. The resulting variation of the sideband phases is:

$$\begin{aligned}\phi_m(\alpha, \beta, \gamma) &= \phi_m(\alpha, \beta, 0) \\ &\quad - \sum_{k\neq0}\frac{\omega_k(\alpha, \beta, 0)(\exp(-{\rm i}k\gamma) - 1)}{-{\rm i}k\omega_{\rm r}} + m\gamma,\end{aligned} \tag{12}$$

where we have written the phases explicitly as functions of the three angles. By contrast, the sideband intensities $A_m$ are independent of $\gamma$.

Equation (10) is then substituted into Eq. (9), while noting that in the latter the shift evolution is in the opposite sense, to give

$$\begin{aligned}\hat{\tilde{H}}(t) = \omega_1 \sum_{m=-\infty}^{+\infty} A_m \hat{R}_z(\phi_{\rm p}(t) - \phi_m - \Omega_{\rm iso}t - m\omega_{\rm r}t) \\ \times \hat{I}_x \hat{R}_z(\phi_{\rm p}(t) - \phi_m - \Omega_{\rm iso}t - m\omega_{\rm r}t)^{-1}.\end{aligned} \tag{13}$$

If the selective pulse is applied to the $n$th-order sideband, the pulse phase can be expressed as $\phi_{\rm p}(t) = (\Omega_{\rm iso} + n\omega_{\rm r})t$, and the Hamiltonian becomes

$$\begin{aligned}\hat{\tilde{H}}(t) = \omega_1 \sum_{m=-\infty}^{+\infty} A_m \hat{R}_z((n - m)\omega_{\rm r}t - \phi_m) \\ \times \hat{I}_x \hat{R}_z((n - m)\omega_{\rm r}t - \phi_m)^{-1}.\end{aligned} \tag{14}$$

### C. Low-power approximation

Caravatti *et al.* showed that if the applied RF field is much lower than the spinning rate, i.e., $\omega_1 \ll \omega_{\rm r}$, the time-dependent terms in the sideband expansion of the RF field in Eq. (14) can be discarded. It is worth noting that the same logic is used to discard the nonresonant term in the RF field of a conventional pulse on transforming from the laboratory reference frame to the standard rotating frame. The resulting Hamiltonian acquires a very simple form

$$\overline{\hat{\tilde{H}}} = \omega_1 A_n \hat{R}_z(-\phi_n)\hat{I}_x \hat{R}_z(-\phi_n)^{-1}, \tag{15}$$

which represents a simple RF pulse with phase $-\phi_n$ and an applied magnetic field that is scaled down by the relative

intensity of the irradiated sideband $A_n$. Note that if the pulse is applied for a time $t_p$ the magnetization of the spins is rotated by a flip angle $\omega_1 A_n t_p$. Despite the pulse being applied to a single sideband, the irradiation is transmitted to the *whole pattern*.

The scaling of the power reflects the fact that the instantaneous shift of the spin has a value such that the magnetization is able to be rotated by the RF field only for a fraction of the duration of the pulse. This fraction is, of course, given by the fraction of the rotor period within which the spin 'occupies' the irradiated sideband, namely $A_n$.

## III. SINGLE-SIDEBAND INVERSION BY ADIABATIC PULSES

### A. Swept-frequency pulses in the jolting frame

In light of the above discussion, we realize that the pattern of sideband intensities varies with the crystallite orientation and so if we irradiate a particular sideband with a conventional pulse, it will be impossible to achieve the same rotation angle for all the crystallites simultaneously. However, we can, in principle, obtain a perfect 180° rotation by applying a swept-frequency adiabatic pulse to a particular sideband. The beauty of such a single-sideband selective pulse ($S^3AP$) is that, provided the RF field is above a certain threshold value, so that the adiabaticity condition is satisfied, we obtain perfect inversion regardless of the exact value of the field.

For an adiabatic frequency sweep through the $n$th sideband, the Hamiltonian in the jolting frame has a similar form to Eq. (14):

$$\hat{\tilde{H}}(t) = \omega_1(t) \sum_{m=-\infty}^{+\infty} A_m \hat{R}_z(\phi(t) + (n-m)\omega_r t - \phi_m) \times \hat{I}_x \hat{R}_z(\phi(t) + (n-m)\omega_r t - \phi_m)^{-1}. \quad (16)$$

The differences are that the amplitude profile of the pulse $\omega_1(t)$ is now time dependent, and that we have also included a phase factor $\phi(t)$ that accounts for the frequency sweep.

The Hamiltonian in Eq. (16) describes a mechanism for adiabatic inversion in MAS solids which is radically different from the adiabatic schemes commonly employed in solid-state NMR (e.g., SHAPs). This is illustrated in Fig. 2, which sketches the two alternative ways in which $S^3AP$ and SHAP achieve broadband inversion of a single crystallite.

A traditional adiabatic pulse sweeps through a range of frequencies that is much greater than the entire spectrum (i.e., a SHAP in MAS solids typically sweeps through 1–10 MHz). This is indicated in (a) which shows the spectrum of a single crystallite with an axially-symmetric SA tensor and where the arrow indicates the direction and range of the sweep. By comparison, the $S^3AP$ sweeps through a single sideband, in this case the centerband, as shown (b). The magnetization trajectories induced by the two pulses are very different, as shown by the grapefruit diagrams for a SHAP in (c), and for the $S^3AP$ in (d). The variations of the $z$-magnetization have been extracted and are shown in (e)–(f). During a SHAP, the magnetization follows a similar pathway to that expected for inversion of a solution-state system (e), where the deviations can be explained by the perturbing effect of the MAS modulation of the SA on the effective field during the sweep. It is therefore possible to predict the inversion performance by reference to the traditional adiabatic condition,[9] while accounting for the MAS, or performing a more sophisticated calculation in a superadiabatic frame of Ref. 26. By contrast, the path due to the $S^3AP$ (f) is more complicated, and if analyzed in the standard way appears to be nonadiabatic. However, as can be seen in the plot of the $z$-magnetization against time, the motion can be separated into a smooth inversion upon which is superimposed a rapid oscillation. As detailed in the following sections, the rapid oscillations may be neglected, leaving the smooth variation which is indeed adiabatic.

### B. Low-power adiabatic pulses

We can now apply a variation of the low-power approximation to simplify the Hamiltonian. There are two conditions that must be met in this case: first, as before the RF power must be low enough so that the neighboring sidebands are unaffected ($\omega_1(t) \ll \omega_r$); and second, the range of frequencies through which we sweep must only contain the chosen sideband. Together, these requirements can be quantified to give the following condition which must be met at all times: $|\omega_r - \dot{\phi}(t)| \gg \omega_1(t)$. If this is the case, we can approximate Eq. (16) with the first-order average Hamiltonian:

$$\overline{\hat{\tilde{H}}} = \omega_1(t) A_n \hat{R}_z(\phi(t) - \phi_n) \hat{I}_x \hat{R}_z(\phi(t) - \phi_n)^{-1}. \quad (17)$$

In complete analogy with the result for a square pulse, this represents a swept-frequency pulse in which the RF field has been scaled down by the intensity of the irradiated sideband. As was seen in Fig. 2, the response of the density operator can be separated into two parts: a smooth variation which, if adiabatic, delivers complete broadband inversion, and a rapid oscillation which is superimposed upon the former variation. The term that is retained in the low-power approximation is responsible for the former, while the oscillating fields produce the latter.

### C. Adiabaticity conditions

When dealing with adiabatic pulses in NMR, an adiabaticity condition is often used to determine whether or not perfect inversion is achieved on a given spectrum.

Traditionally, this condition states that efficient inversion is achieved whenever the effective field of the pulse $\omega_{eff}(t)$ is greater than the rate of change $d\theta(t)/dt$ of its tilt angle from the $z$-axis of the modulated frame.[9] This criterium is expressed in terms of a quality factor $Q$:

$$\frac{1}{Q} = \left| \frac{\dot{\theta}(t)}{\omega_{eff}(t)} \right|. \quad (18)$$

In this formalism, good inversion is predicted when $Q \gg 1$. Recently, we have introduced the notion of superadiabaticity and illustrated the fact that the traditional $Q$ factor

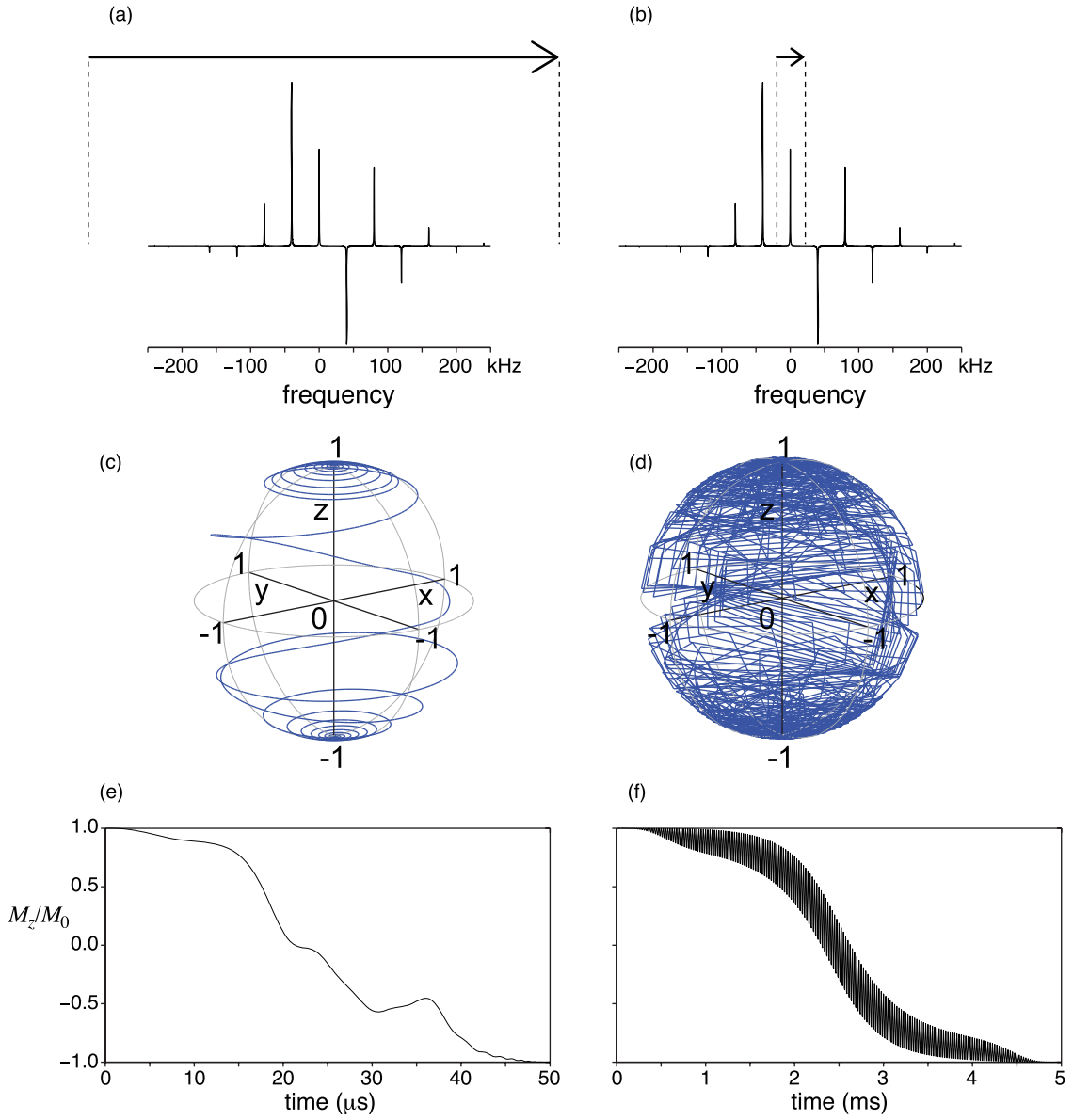


FIG. 2. Comparison of SHAP (left) and $S^3AP$ (right) in obtaining broadband inversion of a single crystallite with an axially-symmetric SA tensor under MAS. The simulated spectra (a-b), magnetization trajectories (c-d), and the variation of the $z$-magnetization during the pulse (e-f) are shown for a SHAP (a,c,e) and a $S^3AP$ (b,d,f). The anisotropy of the SA tensor is 100 kHz, and the rate of MAS is 40 kHz. The Euler angles relating the PAF to the rotor frame of the single crystallite are $(\alpha, \beta, \gamma) = (0, \theta_M, 0)$, where $\theta_M$ is the magic angle. The SHAP is a tan/tanh pulse (Refs. 10 and 24) which sweeps through 10 MHz in 50 $\mu$s with a peak RF field of 200 kHz, while $S^3AP$ is a WURST-20 pulse (Ref. 7) which sweeps through 30 kHz in 5 ms with an RF field of 10 kHz. The simulations were performed using SPINEVOLUTION (Ref. 25).

is not a proper indicator of the adiabaticity of a pulse.[26] We have shown that efficient resonance inversion can be achieved whenever the magnetization is sufficiently well locked, not by the effective field in the conventional modulated frame, but rather by the effective field $\omega_{\mathrm{eff,k}}(t)$ in an adiabatic representation $(x_k, y_k, z_k)$. This has led us to re-state the adiabaticity condition in terms of a superadiabatic quality factor ${}^sQ$, which monitors the minimal rate of change $\mathrm{d}\theta_k(t)/\mathrm{d}t$ of the tilt angle of the effective field from the $z$-axis of the $k$th modulated frame:

$$\frac{1}{{}^sQ} = \min_k \frac{1}{Q_k} = \left| \frac{\dot{\theta}_k(t)}{\omega_{\mathrm{eff,k}}(t)} \right|. \tag{19}$$

Good inversion is predicted when ${}^sQ \gg 1$.

The above equations introduce values for the effective fields, above which all RF pulses achieve complete inversion. For a given pulse, this means that there is a value of $\omega_1$ above which inversion is 100% efficient. In the case of single-sideband inversion, in conditions where the low-power approximation applies, the RF intensity is scaled down by $A_n^{(i)}$, which represents the intensity of the irradiated sideband for the crystallite $i$. This results in the reduction of the quality factor ${}^sQ$. A new adiabaticity condition needs thus to be defined, which applies to each specific crystallite. This means that, for a certain set of pulse parameters, perfect inversion will be observed for all crystallites for which the intensity of the irradiated sideband is above a certain value.

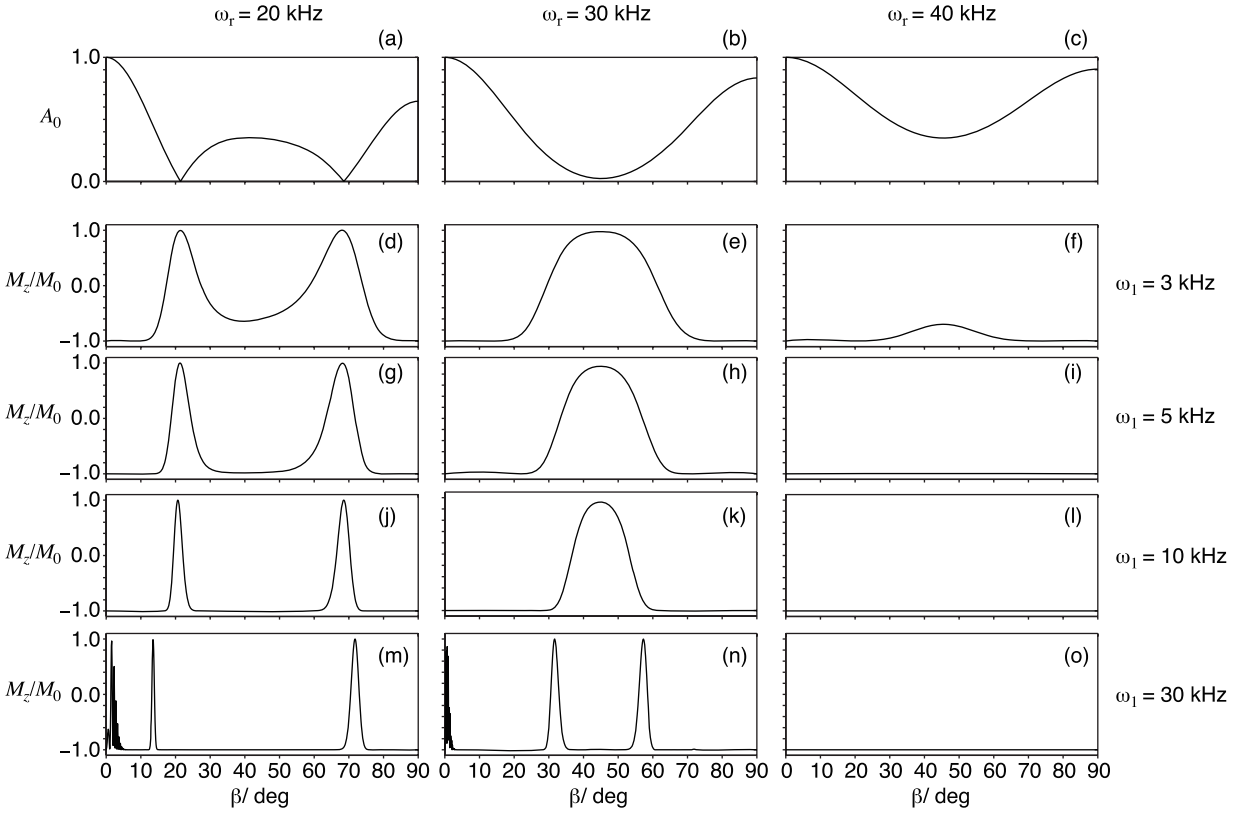


FIG. 3. Illustration of the correlation between the intensity of the centerband $A_0$ and the degree of expected inversion for an axially-symmetric SA tensor. The plots in (a)–(c) show $A_0$ for an anisotropy of 100 kHz as a function of the Euler angle $\beta$ at spinning frequencies of 20, 30, and 40 kHz. The other plots give the value of $M_z$ as a function of $\beta$ at RF powers of (d)–(f) 3 kHz, (g)–(i) 5 kHz, (j)–(l) 10 kHz, and (m)–(o) 30 kHz, as calculated with SPINEVOLUTION (Ref. 25). The pulse is a WURST-20 (Ref. 7) which sweeps through a range of 30 kHz in 5 ms.

When deciding which sideband to irradiate, it should be noted that some crystallites possess sideband patterns in which some of the sidebands have zero intensity. For example, we may consider the case of a crystallite with an axially symmetric shift tensor. If the Euler angle $\beta$ relating the principle axis frame to the rotor frame has a value of zero, the shift is equal to the isotropic value at all times during the rotor period, and so all the sideband intensity is concentrated solely in the centerband. In this case, obtaining any degree of inversion is only possible if we irradiate the centerband. In addition, if we consider an arbitrary crystallite, it is found that increasing the spinning rate of the sample increases the intensity of the centerband at the expense of the other sidebands. Both of these observations indicate that in order to achieve complete inversion of the sideband pattern of the *whole powder*, the best choice of irradiated sideband is the centerband. Therefore, in order to obtain complete inversion of the powder, it is necessary to choose experimental conditions for which every crystallite is inverted.

Figure 3 shows the intensity of the centerband as a function of $\beta$ at different spinning speeds for a single spin with an axially-symmetric shift tensor of 100 kHz anisotropy. For such a tensor, the centerband intensity is a function of $\beta$ only. The inversion profiles of an adiabatic pulse as a function of this angle were calculated using SPINEVOLUTION.[25] The chosen pulse was a WURST-20 which swept through 30 kHz in 5 ms.[7]

For all spinning frequencies, it can be seen that increasing the RF field results in complete inversion for a greater proportion of crystallites with lower-intensity centerbands, as can be seen in Figs. 3(d), 3(g), and 3(m). At 20 kHz MAS some crystallite orientations have a centerband intensity close to zero, as shown in (a), and consequently the adiabaticity condition cannot be fulfilled for these angles. Similar behavior is observed at 30 kHz MAS, in which the minimum centerband intensity is 3%, where increasing the RF power from 3 kHz in (e) to 5 kHz (h), and then 10 kHz (k) gives total inversion for a greater range of $\beta$ angles.

At higher spinning speeds, a greater proportion of the spectral intensity is located in the centerband, and so the minimum centerband intensity present in the powder is greater. Therefore, the adiabatic condition for crystallites with the minimum centerband intensity can be reached with a lower RF field. For example, perfect inversion can be obtained under 40 kHz MAS by increasing the RF power from 3 kHz, as shown in (f), to 5 kHz as shown in (i). Increasing the power further to 10 kHz (l), and then to 30 kHz (o) still provides perfect inversion. Furthermore, increasing the spinning rate increases the separation between neighboring sidebands, which means that we remain within the low-power approximation with a higher-power RF pulse. If we increase the RF power to 30 kHz, as is shown in (m), (n), and (o) we start to see some counter-intuitive behavior, in that some crystallites experience a different degree of inversion from what is expected. The most striking example is at 30 kHz MAS in

(n), where the crystallite at $\beta = 45^\circ$ with a low-intensity centerband experiences complete inversion, whereas the crystallites at 32 and 58° are not inverted at all. These observations can be explained by noting that at this RF power, the low-power approximation is violated and the neighboring sidebands must be taken into account, as detailed in the following section.

## IV. SINGLE-MODE FLOQUET REPRESENTATION IN THE JOLTING FRAME

### A. Effective Hamiltonian in the jolting frame

Although the evolution of the RF field is rather complicated, the overall effect of the Hamiltonian beyond the low-power approximation can be studied either by applying the average Hamiltonian theory (AHT),[27] or single-mode operator-based Floquet theory,[28–31] where the Hamiltonian is approximated by a time-independent effective Hamiltonian $\overline{\hat{H}}$. The use of AHT is valid only if we calculate the density operator at multiples of the period of the Hamiltonian.[30] However, in practice the RF amplitude and phase of the adiabatic pulse are digitized more finely in order to generate expected inversion, and the restriction to stroboscopic sampling every rotor period is too restrictive. For this reason, we adopt Floquet theory to explain the effects of the pulse. The derivation of the effective Hamiltonian is generally a very complex task which is well-documented in the literature,[28–31] and will not be repeated here. However, we will use the final expressions.

To proceed, we must first express the Hamiltonian in Eq. (13) in the following form:

$$\hat{\tilde{H}}(t) = \sum_{p=-\infty}^{+\infty} \hat{H}_p \exp(\mathrm{i}p\omega_\mathrm{r}t), \tag{20}$$

where $\hat{H}_p$ are operators satisfying the relation $\hat{H}_{-p} = \hat{H}_p^*$. Writing Eq. (13) in terms of the raising and lowering operators $\hat{I}_+$ and $\hat{I}_-$ gives the desired result, with $\hat{H}_p$ being given by:

$$\hat{H}_p = \tfrac{1}{2}\omega_1(A_{n+p}\exp(+\mathrm{i}\phi_{n+p})\hat{I}_+ + A_{n-p}\exp(-\mathrm{i}\phi_{n-p})\hat{I}_-), \tag{21}$$

where $p = m - n$.

The effective Hamiltonian $\overline{\hat{H}}$ is equal to a sum of effective Hamiltonians $\overline{\hat{H}^{(i)}}$ of orders $i$:[31]

$$\overline{\hat{H}} = \sum_{i=1}^{\infty} \overline{\hat{H}^{(i)}}. \tag{22}$$

The first three terms in the expansion of the effective Hamiltonian can now be written in terms of $\hat{H}_p$:

$$\overline{\hat{H}^{(1)}} = \hat{H}_0, \tag{23}$$

$$\overline{\hat{H}^{(2)}} = -\frac{1}{2}\sum_{p\neq 0}\frac{[\hat{H}_{-p}, \hat{H}_p]}{p\omega_\mathrm{r}}, \tag{24}$$

$$\overline{\hat{H}^{(3)}} = -\frac{1}{2}\sum_{p\neq 0}\frac{[[\hat{H}_0, \hat{H}_p], \hat{H}_{-p}]}{p^2\omega_\mathrm{r}^2} - \frac{1}{3}\sum_{p\neq 0}\sum_{p'\neq p\neq 0}\frac{[[\hat{H}_{p-p'}, \hat{H}_{p'}], \hat{H}_{-p}]}{pp'\omega_\mathrm{r}^2}. \tag{25}$$

The sideband phases can be rewritten according to Eq. (11). For an axially-symmetric SA tensor, such as we are studying here, all the terms are independent of $\alpha$. The first term is simply the sideband phase for $\gamma = 0$, and for an axially-symmetric tensor can only take the values 0 or $\pi$. It is therefore removed from the above expression, and accounted for by allowing the sideband intensities $A_m$ to be either positive ($\phi_m(\alpha, \beta, 0) = 0$) or negative ($\phi_m(\alpha, \beta, 0) = \pi$). The second term is the phase acquired due to the SA evolution up to time $\gamma/\omega_\mathrm{r}$. It is constant for all sidebands of a given crystallite, and only affects the absolute phase of the RF field. It is therefore neglected in the following. The third term, however, is very important as it determines how the relative phase varies across the sideband pattern.

For an axially-symmetric SA tensor, the first three effective Hamiltonians are:

$$\overline{\hat{H}^{(1)}} = \omega_1(t)A_n\hat{R}_z(\phi(t) - \phi_n)\hat{I}_x\hat{R}_z(\phi(t) - \phi_n)^{-1}, \tag{26}$$

$$\overline{\hat{\tilde{H}}^{(2)}} = \frac{\omega_1(t)^2}{4\omega_\mathrm{r}}\sum_{p\neq 0}\frac{A_{n+p}^2 - A_{n-p}^2}{p}\hat{I}_z, \tag{27}$$

$$\overline{\hat{\tilde{H}}^{(3)}} = -\frac{\omega_1(t)^3}{8\omega_\mathrm{r}^2}\sum_{p\neq 0}\frac{A_0(A_{n-p} - A_{n+p})^2}{p^2}\hat{R}_z(\phi(t) - \phi_n)\,\hat{I}_x\hat{R}_z(\phi(t) - \phi_n)^{-1} - \frac{\omega_1(t)^3}{12\omega_\mathrm{r}^2}\sum_{p\neq 0}\sum_{p'\neq p\neq 0}\frac{(A_{n-p} - A_{n+p})(A_{n-p'}A_{n+p-p'} - A_{n+p'}A_{n-p+p'})}{pp'}\hat{R}_z(\phi(t) - \phi_n)\hat{I}_x\hat{R}_z(\phi(t) - \phi_n)^{-1}, \tag{28}$$

assuming that the time variation of the sweep phase $\phi(t)$ and the amplitude profile $\omega_1(t)$ is slow compared to the oscillation due to the sample rotation. Note that the slow time dependence of $\phi(t)$ and $\omega_1(t)$ results in a time variation of all the terms of the average Hamiltonian during the pulse. More details regarding the derivation can be found in the Appendix.

If the low-power condition is not met at all times, the higher order terms may come into play. The second-order

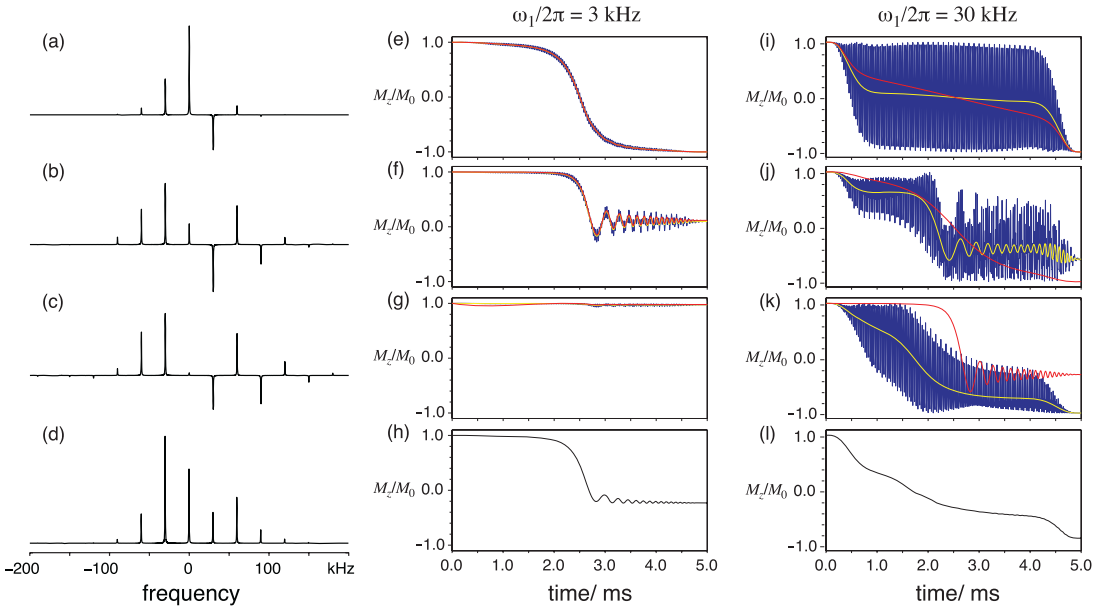


FIG. 4. Simulated variation of the $z$-magnetization of selected crystallites during an adiabatic pulse. The simulated sideband patterns for three crystallites (a)–(c) and the powder (d) are calculated for an axially-symmetric shift tensor of 100 kHz anisotropy, spinning with a MAS rate of 30 kHz. The three crystallites differ in the value of $\beta$ which relates the principal axis frame to the rotor frame; the other two angles are both zero. The values of $\beta$ are (a) 10°, (b) 30°, and (c) 45°. (e)–(l) Simulated comparison of the variation of the $z$-magnetization of the selected crystallites and powder during an $S^3$AP (WURST–20 sweeping through 30 kHz in 5 ms) with two different RF field strengths, with the expected variation if the low-power approximation were valid. (e)–(h) Inversion profiles for a pulse with $\omega_1/(2\pi) = 3$ kHz. (i)–(l) Inversions produced with a field of $\omega_1/(2\pi) = 30$ kHz. The profiles for the single crystallite are shown in blue. Averaging over the angle $\gamma$ gives the profiles in yellow, while the profiles generated assuming the low-power approximation are in red. The average over the powder was calculated using 109 $(\alpha, \beta)$ pairs following the Lebedev octant scheme in (d) (Ref. 32). The superadiabatic and traditional quality factors are calculated for each crystallite accounting for the scaling of the RF field. The numerical values ($^s Q$ and $Q$) for the combination of crystallites and RF field shown are: (e) 264 and 6.71, (f) 0.97 and 0.37, (g) 0.43 and $6.7 \times 10^{-3}$, (i) $9.67 \times 10^5$ and 35, (j) $1.15 \times 10^6$ and 37, and (k) 1.51 and 0.67. See text for further details.

average Hamiltonian simply represents a Bloch–Siegert shift,[19] the effect of which, in the absence of relaxation, is to shift the time at which the $z$-magnetization passes through zero. We observe that if the sideband intensities are symmetrical about the irradiated sideband (that is $A_{n-p} = A_{n+p}$ for all $p$), this term is zero.

The third-order term represents an RF field, and is of more interest in the present discussion. We note that it is applied along the same axis as the first-order field, and so can add either constructively or destructively to the latter. Both of these fields retain the time-dependent phase $\phi(t)$ of the adiabatic sweep, and so the total Hamiltonian represents an adiabatic pulse with a modified RF field acting on a single, isolated, isotropic spin whose offset has been shifted by the Bloch–Siegert term. We note that second-order effective Hamiltonian depends on the difference of the squares of pairs of sideband intensities, and would affect the degree of inversion only under very high-power irradiation $(\omega_1 \gg \omega_r)$.

It is important to note that the *size* of the RF field and the Bloch–Siegert shift are independent of $\gamma$, the consequence of which is that all crystallites within a given carousel experience the same degree of inversion.

## B. Effects of neighboring sidebands

The most obvious way of obtaining the maximum degree of inversion in the spectrum of the powder is to increase the RF field so that the adiabatic condition is fulfilled by a greater quantity of the crystallites with low centerband intensities. However, in practice there is a limit to this, since if the RF field is increased to the point where the low-power approximation is no longer valid, we must consider the effect of the neighboring sidebands. It should be noted that even though the neighboring sidebands still lie outside the band width of the pulse, this does not mean that they do not interfere with the irradiation of the centerband.

Figure 4 shows the simulated time variation of the $z$-magnetization during an $S^3$AP. The simulated sideband patterns in (a)–(c), the magnetization trajectories at a low RF field of 3 kHz in (e)–(g), and a high RF field of 30 kHz in (i)–(k) are given for three crystallites of different orientations. Also shown are the sideband pattern of the powder in (d) and the time profiles of the magnetization during the pulse at 3 kHz (h), and 30 kHz (l). For the plots generated using a field of 3 kHz the low-power approximation is valid and, for all three cases, the magnetization follows the path expected if only the centerband contributes to the irradiation, as seen in (e)–(g). Note that for the profiles in generated by the crystallite, there is an oscillatory motion superimposed on the overall variation of the magnetization from $+z$ to $-z$, which is due to interference from the neighboring sidebands. However, for a given carousel, these oscillations are cancelled by averaging over $\gamma$;[23] the resulting plots are also shown in Fig. 4.

Increasing the RF power of the WURST to 30 kHz gives the magnetization time profiles shown in Figs. 4(i)–4(k), with the corresponding profiles calculated from considering

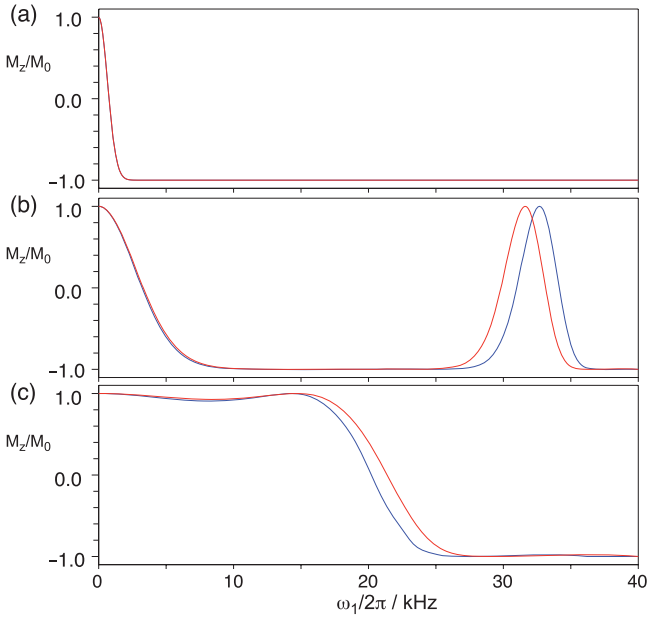


FIG. 5. Simulations of the $z$-magnetization present after the WURST-20 pulse as a function of RF field for the three crystallites shown in Fig. 4 [where $\beta$ is, respectively, (a) 10°, (b) 30°, and (c) 45°]. The curves showing the profile calculated for the crystallites are in blue, whereas in red the profiles calculated using the effective Hamiltonian expansion of Eq. (A1), truncated at the second order sidebands, are in red. In panel (a), the blue and red lines sit directly on top of each other.

only the centerband. First, it can be seen that the amplitude of the oscillations superimposed upon the smooth variation is much greater, reflecting the greater degree of interference from the neighboring sidebands. However, it is still removed by averaging over $\gamma$. Secondly, it is evident that the increased inference has the effect of modifying the degree of inversion: in the case of (j), the inversion is retarded compared to the calculation resulting from the low-power approximation, whereas in (k) it is enhanced to give complete inversion. The numerical values of the superadiabaticity factors (${}^s Q$) can be calculated assuming the low-power approximation, and are given for the six combinations of crystallite orientation and RF power. For the three examples at an RF field of 3 kHz, the superadiabaticity factors provide an accurate indication of the expected degree of inversion, reflecting the validity of the low-power adiabatic approximation in these cases. As for the examples at an RF field of 30 kHz shown in Figs. 4(j) and 4(k), the calculated values of ${}^s Q$ clearly indicate that the low-power approximation fails to account for the observed degree of inversion.

The higher-order effects can be more readily seen from the RF profiles of the pulse acting on the three crystallites of the 100 kHz axially-symmetric SA tensor, which are shown in Figs. 5(a)–5(c).

The origin of the interference effects can be more easily explained by reference to the RF profiles for the three crystallites which give $M_z$ following the pulse as a function of RF field; these are shown for the three crystallites in Fig. 5. The crystallite for which $\beta = 10°$ is shown in (a). It can be seen that once the adiabatic condition has been reached, at 2.5 kHz, complete inversion is still observed up to RF powers of 40 kHz. By comparison, the profile of the crystallite with $\beta = 30°$ in (b) exhibits a peak at 32.5 kHz at which no net inversion occurs, which accounts for the retarded inversion observed in Fig. 4(j). However, for the third crystallite with $\beta = 45°$, the profile of which is seen in Fig. 5(c), the adiabatic condition is apparently reached at a lower RF field than expected, resulting in the enhanced inversion seen in Fig. 4(k).

These interference effects can be explained by calculating the higher order effective Hamiltonians given in Eq. (28). Figure 5 also shows the RF profiles that were simulated using the effective Hamiltonian for comparison. For both the second- and third-order effective Hamiltonians, we retained the terms that include the four sidebands that are closest to the centerband, that is $m = -2$ to $m = +2$. The centerband corresponds to $m = 0$, the two first-order sidebands correspond to $m = \pm 1$, and $m = \pm 2$ represent the second-order sidebands.

For the crystallites discussed here, the third-order RF field is of opposite sign to the first-order RF field. As $\omega_1^{\max}$ increases, the former field increases in size relative to the latter until the net field is zero, resulting in the maximum observed in the RF profiles. At higher fields, the third-order term dominates the lower order term, and ensures that the adiabatic condition is reached. In the case of Fig. 5(a), the centerband is large, and so dominates the resultant RF field up to 40 kHz. In Fig. 5(c), however, the centerband is very small, and so the third-order field cancels the first-order field at a low value of $\omega_1^{\max}$. This term then dominates the inversion process, giving enhanced inversion at higher fields. The situation in Fig. 5(b) is intermediate in that the centerband field, being of intermediate size, is not canceled until $\omega_1^{\max}$ reaches 30 kHz.

As a final point, it should be borne in mind that although the effective Hamiltonian calculated here provides an explanation of the observed behavior, the effective Hamiltonian series can only be approximated by the first three terms if $\omega_1^{\max} < \omega_r$. It is frequently the case, however, that the RF powers of interest are either equal to or greater than the rate of MAS, and so the quantitative results must be treated with caution.

## V. FULL ADIABATIC INVERSION IN A POWDER SAMPLE

A summary of the reasoning behind the choice of the best experimental conditions is illustrated by Fig. 6 which shows the extent of inversion of a powder average of the crystallites for the same SA tensor as used for the previous simulations.

The average was performed by summing the inversion results using 109 $(\alpha, \beta)$ crystallite orientations in one octant using the Lebedev scheme.[32] The maximum degree of inversion is observed for spinning rates above 35 kHz, and RF fields below 45 kHz. It can also be seen that for spinning frequencies below half the sweep width of the adiabatic pulse, here 15 kHz, the extent of inversion is poor. The explanation for this observation is that, at such spinning frequencies, the pulse sweeps through more than one sideband, resulting in the complete breakdown of the low-power approximation.

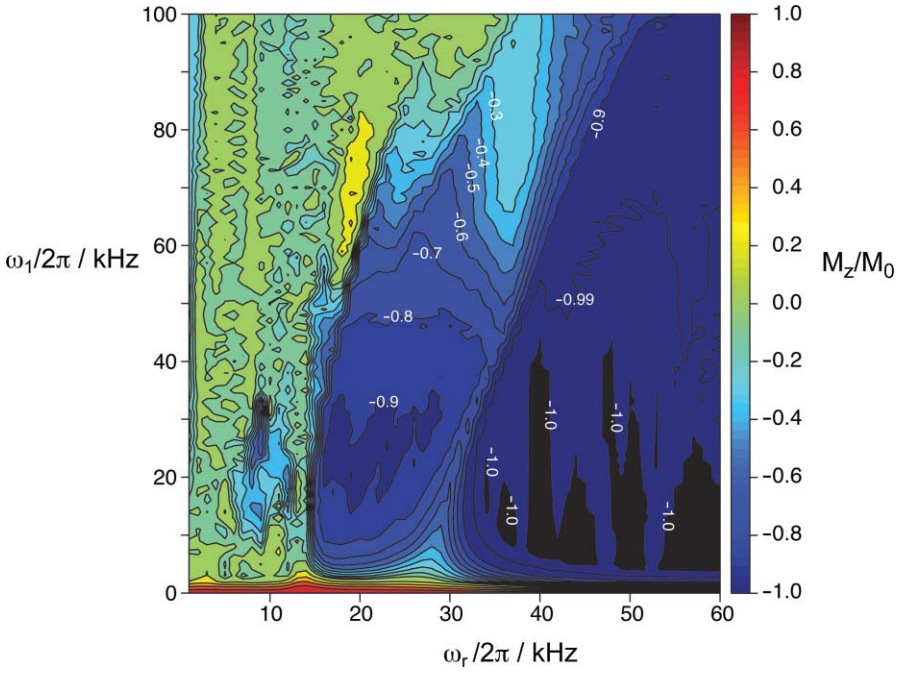


FIG. 6. Contour plot showing the extent of inversion of the sideband pattern of a powder due to the WURST-20 pulse as a function of spinning rate and RF field, calculated with SPINEVOLUTION (Ref. 25). An axially-symmetric SA tensor of 100 kHz was employed in the simulation. The pulse sweeps through 30 kHz in 5 ms. Selected contours are labeled with the values of $M_z/M_0$ that they represent. The sideband pattern is completely inverted at rates of MAS above 35 kHz, and RF field below 45 kHz.

The results of the simulations and experiments presented here allow us to formulate some general recommendations for obtaining the optimum degree of inversion using an $S^3$AP. First, it is beneficial to use the highest rate of MAS that is practicable. The reasons for this are that: (i) a greater spinning rate results in a smaller proportion of the crystallites with low-intensity centerbands, enabling us to reach the adiabatic condition with a lower RF field, and (ii) the greater spacing of the sidebands means that larger RF powers and sweep widths can be employed before we begin to violate the low-power approximation. Secondly, the adiabatic pulse must be designed so that the sweep width is less than twice the spinning frequency, ensuring that only one sideband is swept through, the necessity for which was noted in Sec. V. The remaining parameter to be set is the RF power, which can be optimized with a standard inversion-recovery experiment. 100% inversion can be obtained easily over a large range of parameters.

## VI. EXPERIMENTS

### A. Experimental results

The use of $S^3$AP pulses is illustrated here by two molecules which feature largely anisotropic NMR spectra, as shown in Fig. 7: a diamagnetic selenium compound, **1**, containing four $^{77}$Se spins with a chemical shift anisotropy (CSA) of 53 kHz; and a paramagnetic Tb(III) complex, **2**, where the protons possess large anisotropic shifts of around 1 MHz.[33]

In both cases, hard pulses can only provide incomplete [Fig. 7(b)] or extremely poor inversion [Fig. 7(f)] of the resonance pattern.

For compound **1**, using the recommendations described in the previous section, we selected a WURST–20 adiabatic pulse, and simulated the extent of inversion for a range of $B_1$ fields [Fig. 7(d)], showing that we can obtain complete inversion for fields in between 5 and 15 kHz. This was confirmed experimentally, and Fig. 7(c) shows a quantitative inversion obtained after selective irradiation of the centerband with a WURST–20 with a maximum $B_1$ field of 10 kHz.

Compound **2** presents a more exacting test, due to its extremely short relaxation times and the large inhomogeneous broadening of the lines. A pulse of short duration (i.e., less than 1 ms) is therefore needed, and hyperbolic secant[16] ws found to perform better in this regime. We note that more sophisticated irradiation schemes, such as the one described in Ref. 8, may be adapted more successfully to shorter pulses under fast MAS. Figure 7(h) shows a simulation of the extent of inversion for a pulse of 495 $\mu$s. Despite that no quantitative inversion can be achieved, irradiation in the range 30–60 kHz assures the best results. Indeed, Fig. 7(g) confirms that a 60 kHz hyperbolic secant pulse provided the highest degree of inversion.

### B. Experimental details

$^{77}$Se spectra of compound **1** were recorded on a 500 MHz Avance III Bruker spectrometer, equipped with a 4 mm double-resonance MAS probe spinning at 11 kHz MAS. The pulse sequence comprised cross-polarization[34] from $^1$H to $^{77}$Se followed by a $z$-filter during which the inversion pulse was applied. 2048 transients were recorded for each spectrum with a longitudinal relaxation delay of 5 s.

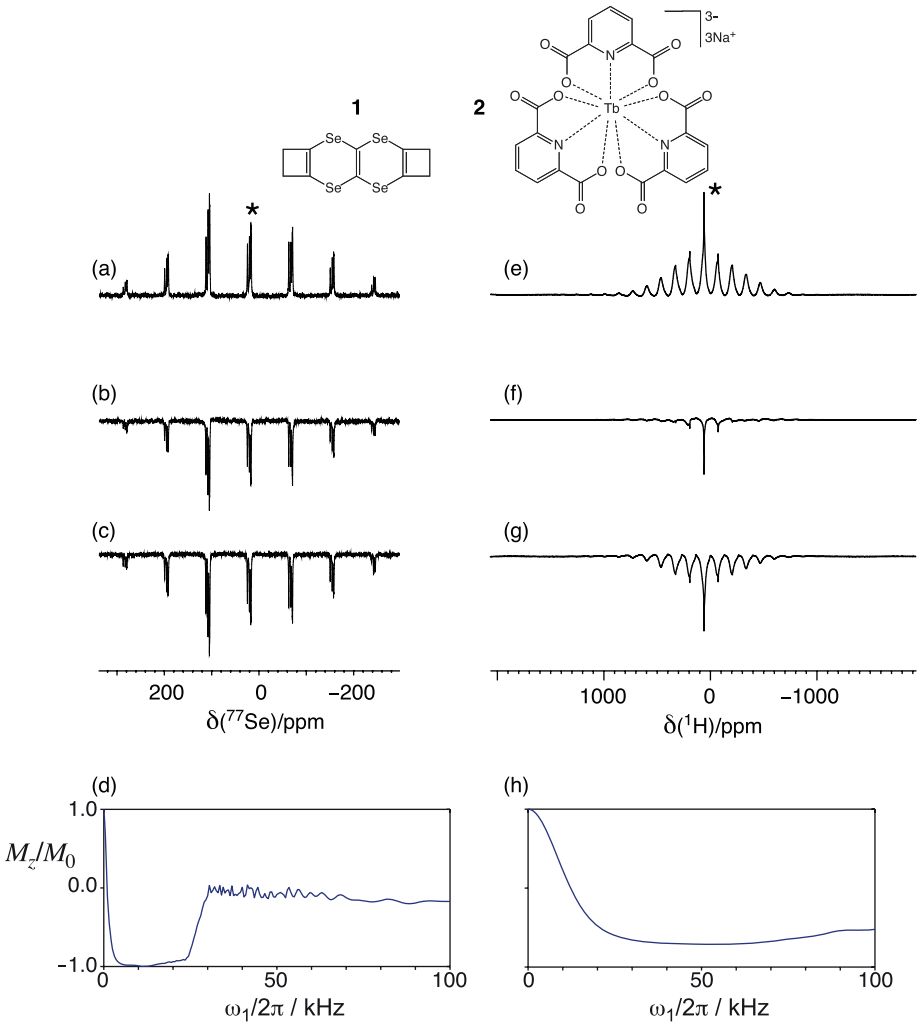


FIG. 7. $^{77}$Se and $^{1}$H NMR spectra of compounds **1** and **2**, under 11 and 60 kHz MAS, respectively. Conventional spectra are shown in (a) and (e). The spectra obtained by inversion with a 69 kHz and 200 kHz hard pulse, respectively are shown in (b) and (f). Spectra obtained by inversion of the centerband using an S$^3$AP are shown in (c) and (g). Simulation of the degree of inversion vs RF power are shown in (d) and (h). The centerbands are indicated with an ∗. Full experimental details are given in Sec. VI B.

Dipolar interactions between the $^{77}$Se and protons were suppressed by using SPINAL-64 decoupling.[35] The reference spectrum is shown in Fig. 7(a), while in Fig. 7(b) is shown the spectrum obtained after a hard pulse inversion with a $B_1$ field of 69 kHz. The spectrum in Fig. 7(c) was obtained after inversion with a WURST–20 pulse which swept through 10 kHz in 5 ms, and had a maximum $B_1$ field of 10 kHz. The superadiabatic quality factor of this pulse is calculated to be 866.

$^{1}$H spectra of compound **2** were recorded on a 500 MHz Avance III Bruker spectrometer, equipped with a 1.3 mm double-resonance MAS probe spinning at 60 kHz MAS.

The reference spectrum is shown in Fig. 7(e). Figure 7(f) shows the spectrum obtained after inversion with a hard pulse of 200 kHz. Figure 7(g) shows the result of selective irradiation of the centerband with a hyperbolic secant of sweep width 70 kHz, duration 495 $\mu$s, and a $B_1$ field of 60 kHz.[16] The superadiabatic quality factor of this pulse is calculated to be $5.56 \times 10^6$. In all three spectra, a double spin echo following a 90° pulse was used to correct for the distorted baseline; the 180° pulses used in the echoes were tan/tanh SHAPs with a $B_1$ field of 200 kHz, and which swept through 10 MHz in 60 $\mu$s (resulting superadiabatic quality factor of 1477). 4096 transients were recorded with a longitudinal relaxation delay of 100 ms.

## VII. CONCLUSIONS

The present work has introduced a framework for representing the Hamiltonian of the spin system in an NMR experiment under MAS.

We have shown that a simple picture of the irradiation process can be obtained by transforming the RF Hamiltonian in the interaction frame of the anisotropic interaction giving rise to the spinning sideband manifold (the "jolting frame"). This representation indicates how the parameters of low-power adiabatic sweeps can be chosen to achieve optimal performance for rotating solids.

We have illustrated with some experimental results how this framework opens new avenues in solid-state NMR for manipulating spin systems with broad SSB manifolds, such as paramagnetic substrates or quadrupolar nuclei.

The principle difficulty encountered with inverting the populations of the nuclear spin states in these materials is that the practical RF powers that are available do not come close to providing the necessary bandwidth. This difficulty traditionally has inhibited the application of many well-established NMR techniques to such samples. We have shown that efficient inversion of an entire sideband family of several hundred kHz can be achieved using low-power, sideband-selective adiabatic pulses. Therefore, the use of $S^3$APs presented here is expected to hold open the door for the development of new NMR techniques for the studies of diamagnetic and paramagnetic species, such as new efficient heteronuclear decoupling schemes, the accurate measurement of site-specific dipolar shift anisotropies in paramagnetic compounds, the enhancement of the central transitions in quadrupolar nuclei via the selective inversion of the satellite transition populations, and the broadband inversion of the whole SSB manifold of a quadrupolar nucleus.

## ACKNOWLEDGMENTS

We acknowledge financial support from the CNRS, Région Centre, Région Rhône-Alpes, the Ministére de la Recherche et l'Enseignement Supérieur, from the Access to research Infrastructures activity in the 6th Framework Program of the EC (Contract No. RII3-026145, EU-NMR), and from the ANR programme blanc (ANR-08-BLAN-0035: PARA-NMR). P.J.G. acknowledges support in part by the National Science Foundation under Grant No. CHE-0616881 and Le Studium, Orlèans, France. Any opinions, findings, and conclusions or recommendations expressed in this material are those of the author(s) and do not necessarily reflect the views of the National Science Foundation (NSF). We thank Dr. O. Maury for supplying the terbium sample **2**, Dr. de Bonneval (LCC Toulouse) for supplying the selenium sample **1**, and Dr. Robin S. Stein (Bruker Biospin, Coventry) for her assistance in the acquisition of the $^{77}$Se spectra.

## APPENDIX: DERIVATION OF THE EFFECTIVE FLOQUET HAMILTONIAN

This appendix contains more details on how the effective Hamiltonians are calculated. The time-dependent Hamiltonian has the form:

$$\hat{\tilde{H}}(t) = \sum_{p=-\infty}^{+\infty} \hat{H}_p \exp(\mathrm{i}p\omega_\mathrm{r}t), \tag{A1}$$

where

$$\hat{H}_p = \tfrac{1}{2}\omega_1(A_{n+p}\exp(+\mathrm{i}\phi_{n+p})\hat{I}_+ + A_{n-p}\exp(-\mathrm{i}\phi_{n-p})\hat{I}_-), \tag{A2}$$

and $p = m - n$.

The first-order effective Hamiltonian can simply be written down as follows:

$$\overline{\hat{H}^{(1)}} = \hat{H}_0 \tag{A3}$$

$$= \tfrac{1}{2}\omega_1[A_n\exp(+\mathrm{i}\phi_n)\hat{I}_+ + A_n\exp(-\mathrm{i}\phi_n)\hat{I}_-] \tag{A4}$$

$$= \tfrac{1}{2}\omega_1 A_n[(\exp(+\mathrm{i}\phi_n) + \exp(-\mathrm{i}\phi_n))\hat{I}_x + \mathrm{i}\,(\exp(+\mathrm{i}\phi_n) - \exp(-\mathrm{i}\phi_n))\hat{I}_y] \tag{A5}$$

$$= \omega_1 A_n[\cos(\phi_n)\hat{I}_x - \sin(\phi_n)\hat{I}_y] \tag{A6}$$

$$= \omega_1 A_n \hat{R}_z(-\phi_n)\hat{I}_x\hat{R}_z(-\phi_n)^{-1}. \tag{A7}$$

The expression for the second-order term is

$$\overline{\hat{H}^{(2)}} = -\frac{1}{2}\sum_{p\neq 0}\frac{[\hat{H}_{-p}, \hat{H}_p]}{p\omega_\mathrm{r}}. \tag{A8}$$

The commutator can be evaluated as follows:

$$[\hat{H}_{-p}, \hat{H}_p] = \tfrac{1}{4}\omega_1^2[A_{n-p}\exp(+\mathrm{i}\phi_{n-p})\hat{I}_+, A_{n-p}\times\exp(-\mathrm{i}\phi_{n-p})\hat{I}_-] + \tfrac{1}{4}\omega_1^2[A_{n+p}\times\exp(-\mathrm{i}\phi_{n+p})\hat{I}_-, A_{n+p}\exp(+\mathrm{i}\phi_{n+p})\hat{I}_+] \tag{A9}$$

$$= \tfrac{1}{4}\omega_1^2\left(A_{n-p}^2 - A_{n+p}^2\right)[\hat{I}_+, \hat{I}_-] \tag{A10}$$

$$= \tfrac{1}{2}\omega_1^2\left(A_{n-p}^2 - A_{n+p}^2\right)\hat{I}_z. \tag{A11}$$

The complete expression for the second-order term is therefore

$$\overline{\hat{\tilde{H}}^{(2)}} = \frac{\omega_1^2}{4\omega_\mathrm{r}}\sum_{p\neq 0}\frac{A_{n+p}^2 - A_{n-p}^2}{p}\hat{I}_z. \tag{A12}$$

The expression for the third-order effective Hamiltonian is:

$$\overline{\hat{H}^{(3)}} = -\frac{1}{2}\sum_{p\neq 0}\frac{[[\hat{H}_0, \hat{H}_p], \hat{H}_{-p}]}{p^2\omega_\mathrm{r}^2} - \frac{1}{3}\sum_{p\neq 0}\sum_{p'\neq p\neq 0}\frac{[[\hat{H}_{p-p'}, \hat{H}_{p'}], \hat{H}_{-p}]}{pp'\omega_\mathrm{r}^2}. \tag{A13}$$

The evaluation of the $p$th term in the first sum gives:

$$-\frac{[[\hat{H}_0, \hat{H}_p], \hat{H}_{-p}]}{2p^2\omega_\mathrm{r}^2} = \frac{A_n\omega_1^3}{8p^2\omega_\mathrm{r}}[A_{n-p}A_{n+p}\exp(\mathrm{i}(\phi_n - \phi_{n-p} - \phi_{n+p})) - A_{n+p}^2\exp(-\mathrm{i}\phi_n)]\hat{I}_- + \frac{A_n\omega_1^3}{8p^2\omega_\mathrm{r}}[A_{n-p}A_{n+p}\times\exp(-\mathrm{i}(\phi_n - \phi_{n-p} - \phi_{n+p})) - A_{n-p}^2\exp(\mathrm{i}\phi_n)]\hat{I}_+. \tag{A14}$$

If we substitute $\phi_k = k\gamma$, the above expression simplifies to:

$$-\frac{[[\hat{H}_0, \hat{H}_p], \hat{H}_{-p}]}{2p^2\omega_\mathrm{r}^2} = \frac{A_n\omega_1^3}{8p^2\omega_\mathrm{r}}[A_{n-p}A_{n+p}\exp(-\mathrm{i}\phi_n) - A_{n+p}^2\exp(-\mathrm{i}\phi_n)]\hat{I}_- + \frac{A_n\omega_1^3}{8p^2\omega_\mathrm{r}}[A_{n-p}A_{n+p}\exp(\mathrm{i}\phi_n) - A_{n-p}^2\exp(\mathrm{i}\phi_n)]\hat{I}_+. \tag{A15}$$

This can then be rewritten in a more convenient form by adding the term $p$ to the term $-p$ and halving the result. This gives an expression in terms of $\hat{I}_x$ and $\hat{I}_y$ as follows:

$$-\frac{\omega_1^3}{8\omega_r^2}\frac{A_0(A_{n-p}-A_{n+p})^2}{p^2}\hat{R}_z(-\phi_n)\hat{I}_x\hat{R}_z(-\phi_n)^{-1}. \quad \text{(A16)}$$

The second sum for the third-order effective Hamiltonian can be evaluated in the same way, with the exception that in the final step, we combine the term labeled $p$, $p'$ with the term $-p$, $-p'$. The final result is

$$-\frac{\omega_1^3}{12\omega_r^2}\frac{(A_{n-p}-A_{n+p})(A_{n-p'}A_{n+p-p'}-A_{n+p'}A_{n-p+p'})}{pp'} \times \hat{R}_z(-\phi_n)\hat{I}_x\hat{R}_z(-\phi_n)^{-1}. \quad \text{(A17)}$$

The third-order effective Hamiltonian is therefore:

$$\overline{\hat{\tilde{H}}^{(3)}} = -\frac{\omega_1^3}{8\omega_r^2}\sum_{p\neq 0}\frac{A_0(A_{n-p}-A_{n+p})^2}{p^2}\hat{R}_z(-\phi_n)\hat{I}_x\hat{R}_z(-\phi_n)^{-1} - \frac{\omega_1^3}{12\omega_r^2}\sum_{p\neq 0}\sum_{p'\neq p\neq 0} \times \frac{(A_{n-p}-A_{n+p})(A_{n-p'}A_{n+p-p'}-A_{n+p'}A_{n-p+p'})}{pp'} \times \hat{R}_z(-\phi_n)\hat{I}_x\hat{R}_z(-\phi_n)^{-1}. \quad \text{(A18)}$$


[1] M. Baldus, Angew. Chem. Int. Ed. Engl. **45**, 1186 (2006).
[2] A. Bockmann, Angew. Chem. Int. Ed. Engl. **47**, 6110 (2008).
[3] C. P. Grey and R. Tycko, Physics Today **62**, 44 (2009).
[4] F. Blanc, C. Coperet, A. Lesage, and L. Emsley, Chem. Soc. Rev. **37**, 518 (2008).
[5] R. Q. Fu and G. Bodenhausen, Chem. Phys. Lett. **245**, 415 (1995).
[6] E. Kupce and R. Freeman, J. Magn. Reson. Ser. A **117**, 246 (1995).
[7] E. Kupce and R. Freeman, J. Magn. Reson. Ser. A **115**, 273 (1995).
[8] E. Kupce and R. Freeman, J. Magn. Reson. Ser. A **118**, 299 (1996).
[9] M. Garwood and L. DelaBarre, J. Magn. Reson. **153**, 155 (2001).
[10] T. L. Hwang, P. C. M. van Zijl, and M. Garwood, J. Magn. Reson. **133**, 200 (1998).
[11] K. Riedel, C. Herbst, J. Leppert, O. Ohlenschlager, M. Gorlach, and R. Ramachandran, J. Biomol. NMR **35**, 275 (2006).
[12] G. Kervern, G. Pintacuda, and L. Emsey, Chem. Phys. Lett. **435**, 157 (2007).
[13] R. Siegel, T. T. Nakashima, and R. E. Wasylishen, J. Magn. Reson. **184**, 85 (2007).
[14] T. T. Nakashima, R. E. Wasylishen, R. Siegel, and K. J. Ooms, Chem. Phys. Lett. **450**, 417 (2008).
[15] T. T. Nakashima, R. Teymoori, and R. E. Wasylishen, Magn. Reson. Chem. **47**, 465 (2009).
[16] J. Baum, R. Tycko, and A. Pines, Phys. Rev. A **32**, 3435 (1985).
[17] K. K. Dey, S. Prasad, J. T. Ash, M. Deschamps, and P. J. Grandinetti, J. Magn. Reson. **185**, 326 (2007).
[18] P. Caravatti, G. Bodenhausen, and R. R. Ernst, J. Magn. Reson. **55**, 88 (1983).
[19] A. Abragam, *Principles of Nuclear Magnetism* (Oxford University Press, Oxford, 1961).
[20] G. Bodenhausen, R. Freeman, and G. A. Morris, J. Magn. Reson. **23**, 171 (1976).
[21] G. A. Morris and R. Freeman, J. Magn. Reson. **29**, 433 (1978).
[22] M. M. Maricq and J. S. Waugh, J. Chem. Phys. **70**, 3300 (1979).
[23] M. H. Levitt, J. Magn. Reson. **82**, 427 (1989).
[24] G. Kervern, A. D'Aleo, O. Maury, L. Emsley, and G. Pintacuda, Angew. Chem. Int. Ed. Engl. **48**, 3082 (2009).
[25] M. Veshtort and R. G. Griffin, J. Magn. Reson. **178**, 248 (2006).
[26] M. Deschamps, G. Kervern, D. Massiot, G. Pintacuda, L. Emsley, and P. J. Grandinetti, J. Chem. Phys. **129**, 204100 (2008).
[27] U. Haeberlen and J. S. Waugh, Phys. Rev. **175**, 453 (1968).
[28] J. H. van Vleck, Phys. Rev. **74**, 1168 (1948).
[29] H. Primas, Rev. Mod. Phys. **35**, 710 (1963).
[30] M. Goldman, P. J. Grandinetti, A. LLor, Z. Olejniczak, J. R. Sachleben, and J. Zwanziger, J. Chem. Phys. **97**, 8947 (1992).
[31] M. Leskes, P. K. Madhu, and S. Vega, "Floquet theory in solid-state nuclear magnetic resonance," Prog. Nucl. Magn. Reson. Spectrosc. **57**, 345 (2010).
[32] M. Edén and M. H. Levitt, J. Magn. Reson. **132**, 220 (1998).
[33] G. Kervern, S. Steuernagel, F. Engelke, G. Pintacuda, and L. Emsley, J. Am. Chem. Soc. **129**, 14118 (2007).
[34] G. Metz, X. Wu, and S. O. Smith, J. Magn. Reson. Ser. A **110**, 219 (1994).
[35] B. M. Fung, A. K. Khitrin, and K. Ermolaev, J. Magn. Reson. **142**, 97 (2000).